The energy response of LaBr$_3$(Ce), LaBr$_3$(Ce,Sr), and NaI(Tl) crystals for GECAM

Pei-Yi Feng[1,2,3] · Xi-Lei Sun[4,5] · Zheng-Hua An[1,2] · Yong Deng[6] · Cheng-Er Wang[7] · Huang Jiang[5] · Jun-Jie Li[6] · Da-Li Zhang[2] · Xin-Qiao Li[2] · Shao-Lin Xiong[2] · Chao Zheng[2,3] · Ke Gong[2] · Sheng Yang[2] · Xiao-Jing Liu[2] · Min Gao[2] · Xiang-Yang Wen[2] · Ya-Qing liu[2] · Yan-Bing Xu[2] · Xiao-Yun Zhao[2] · Jia-Cong Liu[2,3] · Fan Zhang[2] · Hong Lu[1,2]

Abstract

The GECAM series of satellites utilizes LaBr$_3$(Ce), LaBr$_3$(Ce,Sr), and NaI(Tl) crystals as sensitive materials for gamma-ray detectors (GRDs). To investigate the nonlinearity in the detection of low-energy gamma rays and address the errors in the calibration of the E–C relationship, comprehensive tests and comparative studies of the three aforementioned crystals were conducted using Compton electrons, radioactive sources, and mono-energetic X-rays. The nonlinearity test results of the Compton electrons and X-rays demonstrated substantial differences, with all three crystals presenting a higher nonlinearity for X/γ-rays than for Compton electrons. Despite the LaBr$_3$(Ce) and LaBr$_3$(Ce,Sr) crystals having higher absolute light yields, they exhibited a noticeable nonlinear decrease in the light yield, especially at energies below 400 keV. The NaI(Tl) crystal demonstrated an "excess" light output in the 6–200 keV range, reaching a maximum "excess" of 9.2% at 30 keV in the X-ray testing and up to 15.5% at 14 keV during Compton electron testing, indicating a significant advantage in the detection of low-energy gamma rays. Furthermore, we explored the underlying causes of the observed nonlinearity in these crystals. This study not only elucidates the detector responses of GECAM, but also initiates a comprehensive investigation of the nonlinearity of domestically produced lanthanum bromide and sodium iodide crystals.

Keywords LaBr$_3$(Ce) detector · LaBr$_3$(Ce, Sr) detector · NaI(Tl) detector · GECAM · Energy response · Light yield nonlinearity

✉ Xi-Lei Sun
   sunxl@ihep.ac.cn

   Pei-Yi Feng
   fengpeiyi@ihep.ac.cn

   Zheng-Hua An
   anzh@ihep.ac.cn

   Hong Lu
   luh@ihep.ac.cn

1 Particle and Astrophysics Center, Institute of High Energy Physics, Chinese Academy of Sciences, Beijing 100049, China

2 Key Laboratory of Particle Astrophysics, Institute of High Energy Physics, Chinese Academy of Sciences, Beijing 100049, China

3 University of Chinese Academy of Sciences, Chinese Academy of Sciences, Beijing 100049, China

4 Experimental Physics Center, Institute of High Energy Physics, Chinese Academy of Sciences, Beijing 100049, China

5 State Key Laboratory of Particle Detection and Electronics, Institute of High Energy Physics, Chinese Academy of Sciences, Beijing 100049, China

6 School of Nuclear Science and Technology, University of South China, Hengyang 421001, China

7 National Engineering Research Center for Rare Earth, Grirem Advanced Materials Co., Ltd. and General Research Institute for Nonferrous Metals, Beijing 100088, China

1 Introduction

Recent groundbreaking advancements in various branches of astrophysics, such as gravitational waves, fast radio bursts, and cosmic rays have been observed, enabling a new "multi-messenger, multi-wavelength" era in astronomy [1–5]. These discoveries emphasize the importance of efficient detection methods to further understand high-energy astronomical phenomena. Transient gamma-ray sources, including gamma-ray bursts and magnetar flares, play a vital role in the study of astronomy [6–11].

The gravitational wave burst high-energy Electromagnetic Counterpart All-sky Monitor (GECAM) series, comprising satellites GECAM-A/B, GECAM-C, and GECAM-D, was developed to monitor various high-energy electromagnetic events, such as gamma-ray bursts and magnetar flares [12–16]. These satellites employ gamma-ray detectors (GRDs) that utilize different scintillating crystals such as $LaBr_3(Ce)$ and $LaBr_3(Ce,Sr)$ for GECAM-A/B, and a combination of $LaBr_3(Ce)$, $LaBr_3(Ce,Sr)$, and NaI(Tl) to validate new detector technologies for GECAM-C. The fourth satellite, GECAM-D, uses NaI(Tl) crystals, and is scheduled to be launched in early 2024. The main characteristics of the GRDs are listed in Table 1.

GRDs serve as primary detectors in the GECAM payload, and GECAM-A/B utilizes an innovative solution that employs $LaBr_3$ crystals coupled with silicon photomultiplier (SiPM) readout technology (Fig. 1) [14, 15, 17, 18]. $LaBr_3$ crystals are advanced inorganic scintillators known for their high light outputs, excellent energy and timing resolutions, good energy linearity, and short light-decay times. The SiPM, which replaces the conventional photomultiplier tube (PMT), offers advantages such as a simple and compact structure, ease of miniaturization, and efficient readout capability.

For GECAM-C (Fig. 2), the GRDs employ both NaI(Tl) and $LaBr_3$ crystals, which are coupled to the SiPM readout arrays [16, 19]. The NaI(Tl) crystal is a high-performance traditional inorganic scintillator with excellent luminescence properties that provides a good resolution for both X-rays and gamma rays. Inorganic scintillators are widely used as the preferred choice for high-energy X/γ-ray detectors in space owing to their versatility in shaping and sizing, stability, reliability, reasonable cost, inclusion of heavy elements, high density, and efficient detection capabilities for X/γ-rays.

The crystals used in the GECAM satellite series were obtained from the Beijing Glass Research Institute. To optimize the performance of these detectors, it is critical to understand their energy responses. Consequently, we conducted an in-depth study involving X-ray, Compton electron, and gamma-ray tests on the $LaBr_3(Ce)$, $LaBr_3(Ce,Sr)$,
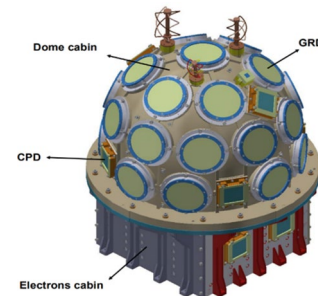

Fig. 1 (Color online) The detector layout schematic of the GECAM-A/B payload. On each satellite, the detectors are designed with a modular approach, consisting of 25 Gamma-Ray Detector (GRD) modules and 8 charged particle detector (CPD) modules
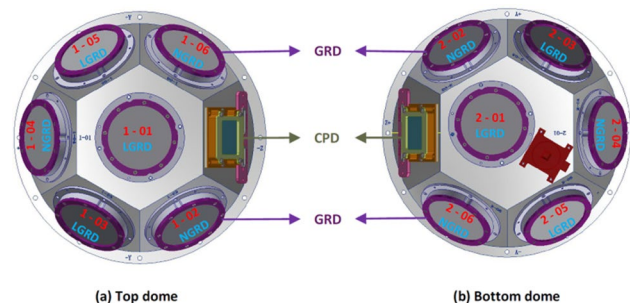

Fig. 2 (Color online) Detector layout schematic of the GECAM-C payload. GECAM-C is composed of two detector domes: top and bottom. Each dome is equipped with different types of GRDs, including NaI-based gamma-ray detectors (NGRDs) and $LaBr_3$-based gamma-ray detectors (LGRDs)

Table 1 The main characteristics of the GRD in GECAM series

GRD parameter	GECAM-A/B	GECAM-C	GECAM-D
Type	$LaBr_3(Ce)$; $LaBr_3(Ce+Sr)$	NaI(Tl); $LaBr_3(Ce)$; $LaBr_3(Ce+Sr)$	NaI(Tl)
Quantity	25	12	5
Area	45.36 cm^2	45.36 cm^2	103.87 cm^2
Energy range	8–2000 keV	15–4000 keV	20–1000 keV
Energy resolution	< 18%@59.5 keV	< 18%@59.5 keV	< 25%@59.5 keV
Detection efficiency	> 50%@8 keV	> 75%@15 keV	> 60%@20 keV
Deadtime	4 μs	4 μs	4 μs

and NaI(Tl) crystals used in these satellites [20–22]. Our findings indicate that the nonlinearity of the three crystals varied when exposed to distinct excitation sources. The LaBr₃(Ce,Sr) crystal exhibited the strongest linear response to Compton electrons in the low-energy range, whereas the NaI(Tl) crystal demonstrated the best linear response to X-rays.

Consistent with previous studies regarding the nonlinearity of iodide crystals [23, 24], domestically produced NaI(Tl) crystals exhibited a light yield "excess" phenomenon, indicating unexpected advantages in the detection of low-energy gamma rays. These insights not only contribute to a better understanding of the detector response of the GECAM series, but also provide invaluable information for evaluating the performance of these domestically produced scintillating crystals in the low-energy range of 3–400 keV [25]. Manufacturers can refer to this study to enhance their understanding of crystal nonlinearity, potentially facilitating the optimization and improvement of the crystal growth processes and doping ratios. Furthermore, this study presents the issue of nonlinearity in crystals for low-energy gamma-ray detection, which is highly significant for addressing errors in detector calibration related to the energy-channel (E-C) relationship. Based on the results of this study, we will further investigate the intrinsic resolution of crystals in future studies.

2 Experimental setup and test procedure

2.1 The wide-angle compton coincidence technology

Figure 3 presents the wide-angle Compton coincidence (WACC) experimental setup, which primarily comprises a radioactive source, a high-purity Germanium (HPGe) detector, the scintillation detector under examination, and a suM) readout technology (subsequent data acquisition system [24, 26–29]. LaBr₃(Ce), LaBr₃(Ce,Sr), and NaI(Tl) cylindrical samples with diameters of 25.4 mm were selected for this study. Silicone oil was used to couple the encapsulated crystals to the PMTs (R6233-100, Hamamatsu Photonics, Japan) [30, 31]. According to the user manual of the BE2020 planar germanium spectrometer manufactured by Canberra, the HPGe crystal had a thickness of 20 mm and a volume of 40,000 mm³, allowing for an energy detection range of 3 keV–3 MeV [32, 33]. Based on the experimental data, the energy resolutions, indicated by the full width at half maximum (FWHM), of the HPGe detector used in this study were determined to be 1.58 keV (⁶⁰Co, 1.33 MeV) and 1.15 keV (¹³⁷Cs, 662 keV).
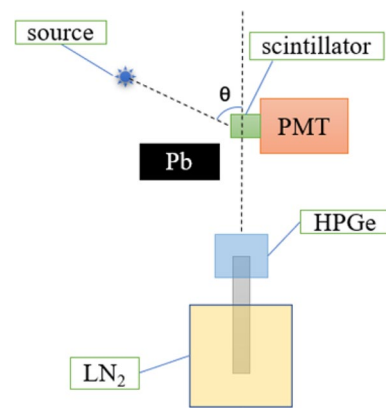

Fig. 3 Schematic diagram of experimental setup for obtaining Compton electrons with a wide energy range

The experiment involved placing a ¹³⁷Cs radioactive source at a quarter-circle position around the center of the crystal, with a distance of 13 cm between the crystal and source. Gamma photons were emitted by the radioactive source via radioactive decay and underwent Compton scattering when they struck the crystal. Consequently, Compton electrons were generated and absorbed by the crystal, whereas certain scattered photons escaped from the crystal and were absorbed by the nearby HPGe detector. The distance between the tested crystal and HPGe detector was maintained at approximately 15 cm. Lead blocks were positioned between the ¹³⁷Cs source and HPGe detector to provide shielding and minimize the incidence of primary gamma photons directly irradiating the HPGe detector. Coincidence events across a broad energy range were obtained by adjusting the position of the radioactive source and varying the angle between the source, crystal, and HPGe detector.

A desktop waveform acquisition device with a 10 bit @ 2 GS/s (interleaved) or 1 GS/s, which was a DT5751 digitizer [34], was utilized in this experiment to collect signals from the crystal and HPGe detectors (Fig. 4). The HPGe detector signal operating at +3500 V underwent shaping and filtering using an ORTEC 572A amplifier before being sent to channel-0 of DT5751. The output signal from the PMT anode operating at +1300 V was routed to channel-1 of DT5751 after the photoelectrons were multiplied by the dynodes. The signals from the crystal and HPGe detectors successively underwent low-threshold discrimination, delayed stretching, and a logical coincidence. The resulting coincidence output signal was utilized as an external trigger for DT5751, which recorded the corresponding coincidence events and generated two data files when triggered externally. The secondary particles produced by Compton scattering were absorbed by the two detectors in a specific order in the time sequence. For a "true

Fig. 4 Diagram of the data acquisition system for coincidence events
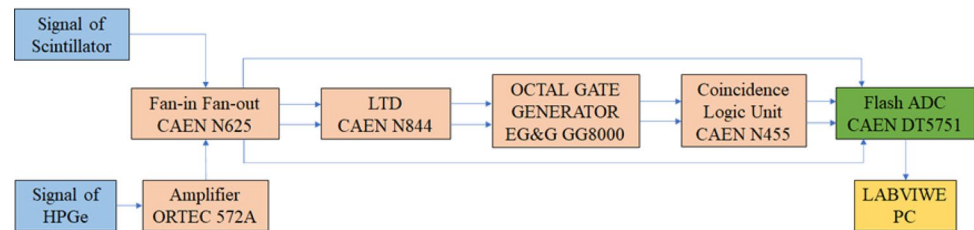
Figure 5 presents the coincidence matrix that represents all the collected data of the events. In Fig. 5a, the horizontal axis represents the energy deposited on the HPGe detector, whereas the vertical axis corresponds to the energy deposited on the LaBr$_3$(Ce,Sr) crystal. As indicated in the Compton scattering formula (Eq. (1)) [24], as the incident angle (θ) of the gamma photon increased, the energy of the Compton electrons in the LaBr$_3$(Ce,Sr) crystal also increased.

$$E_e = E_\gamma - E'_\gamma = \frac{E_\gamma}{1 + \frac{m_e c^2}{E_\gamma (1 - \cos\theta)}}. \tag{1}$$

where E_γ is the energy of the gamma ray radiating from the source, E_e is the energy of the Compton electron, E'_γ is the energy of the scattered photon, θ is the Compton scattering angle, and $m_e c^2$ is the remaining mass energy of the electron. Five scattering angles of θ were chosen during the experiment to obtain data over a broad energy range.

The diagonal points presented in Fig. 5 demonstrate the "true coincidence events" of interest. Each point corresponds to a specific scattering angle, and the combined deposited energies in both the crystal and HPGe detector are constant at 661.6 keV. The uneven "spread" among the diagonal at different energy levels is owing to the diverse energy resolutions of the crystal for Compton electrons. Furthermore, the nonlinear response of the crystal determines the "linearity" of the diagonal. An analysis of the coincidence matrix enabled the extraction of the energy resolution and nonlinear response of the crystal for Compton electrons.

Figure 5 presents the horizontal and vertical lines indicating the accidental coincidence events simultaneously detected by both detectors. The horizontal line represents the finite resolution of the crystal and the vertical line represents the excellent resolution of the HPGe detector. The other points on the graph denote events in which partial energy was deposited in the detector or where detection occurred after scattering through the surrounding materials.

The WACC method accurately measures the energy response and resolution of the crystal detector to the Compton electrons. Before the Compton experiments,
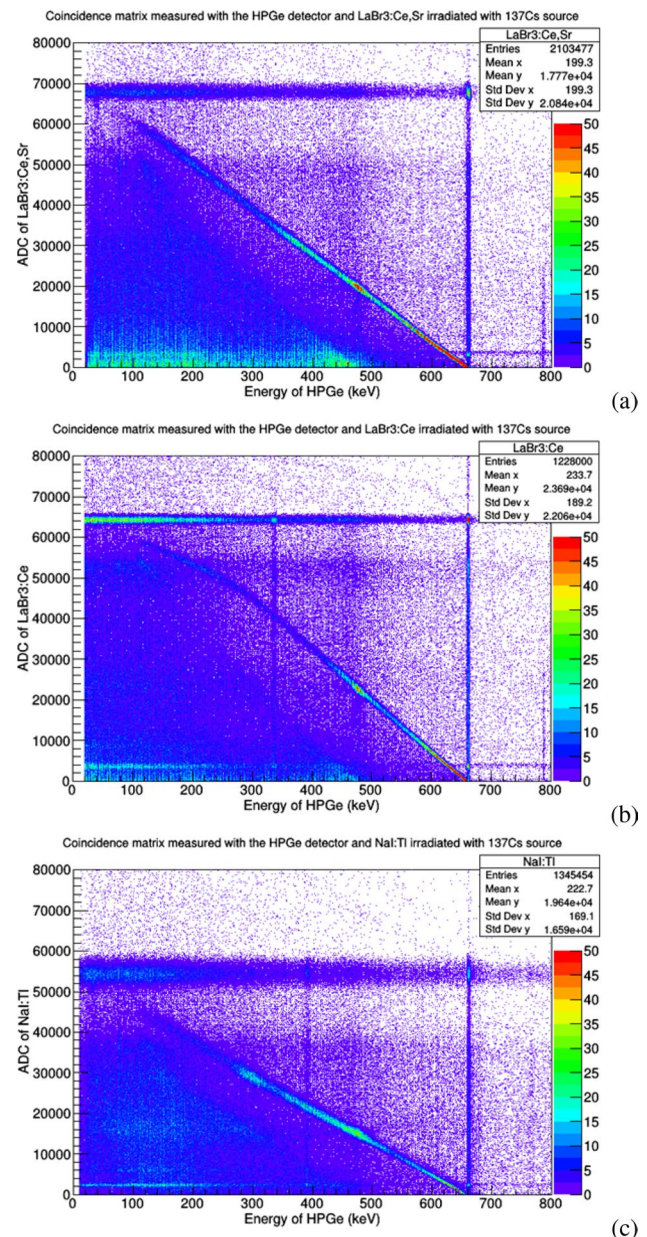

Fig. 5 (Color online) Two-dimensional spectrum of coincidence events in both HPGe and **a** LaBr$_3$(Ce,Sr), **b** LaBr$_3$(Ce), **c** NaI(Tl) with the ^{137}Cs source, that is, the coincidence matrix

it was necessary to calibrate the E-C relationship of the HPGe detector, which can be obtained from the energy spectra of multiple radioactive sources or directly using the vertical lines in the coincidence matrix.

The HPGe detector offers an outstanding energy resolution, making it an excellent standard detector. The energy deposited in the crystal was calculated by subtracting the scattered photon energy in the HPGe detector from the known gamma-ray source energy. In actual data processing, the cut width of the HPGe energy axis must be determined based on the statistics of the Compton scattering event. Within this range, the central value is considered to be the energy deposited in the HPGe detector, and Eq. (2) is used to calculate the energy deposited in the crystal. In this study, cutting was performed along the HPGe energy axis and projected onto the crystal axis.

$$\langle E_{\text{scin}} \rangle = E_\gamma - \langle E_{\text{HPGe}} \rangle \tag{2}$$

where E_γ is the known gamma-ray source energy, $\langle E_{\text{HPGe}} \rangle$ is the deposited energy in the HPGe detector, and $\langle E_{\text{scin}} \rangle$ is the deposited energy in the crystal.

To understand the effect of the cut width or energy window width, we measured the energy resolution of the LaBr₃ (Ce,Sr) crystal to 46.6 keV Compton electrons for different cut widths. The results indicated that the energy resolution remained reasonably stable until a cut width of 4 keV was reached (Fig. 6). Wider cut widths led to a broadened scattering angle range of relevant valid events and an increase in the FWHM of the Compton electron spectrum. Subsequently, the resolution deteriorated. The energy resolution of the HPGe detector was within 1–2 keV, which must be considered when determining a reasonable cut width. It is also essential to ensure a sufficient number of events. Therefore, a cutoff width of 4 keV was used when the energy deposited in the HPGe detector was less than 615 keV. When
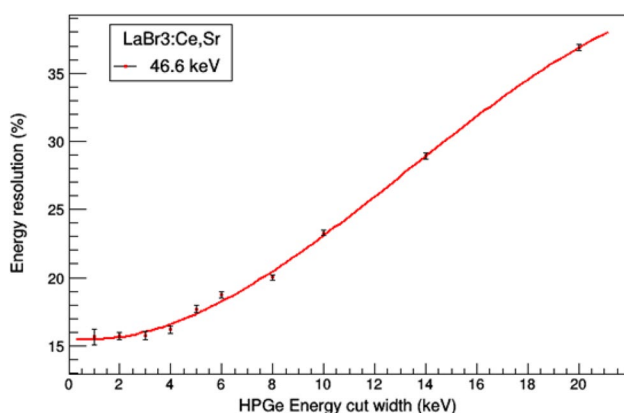
the deposited energy was within 615 to ¯661.6 keV, a cutoff width of 2 keV was selected.

Multiple truncations of the HPGe energy axis were performed to obtain the crystal spectra for various Compton electron energies. Figure 7 illustrates an example of this approach, in which a data range of events from 614 to 616 keV was considered at an HPGe energy of 615 keV with a cut width of 2 keV to produce the Compton electron spectrum (Fig. 7b). A Gaussian-shaped, single-energy electron peak was visible and fitted with a Gaussian function, returning an energy resolution of 15.81 ± 0.25% for the 46.6 keV Compton electrons in the LaBr₃(Ce,Sr) crystal.

Atoms or molecules are excited when incident particles deposit energy in a crystal, leading to the emission of scintillation photons with wavelengths similar to those of visible light [35]. The light yield, defined as the number of scintillation photons per unit of energy deposited in the crystal, is described by Eq. (3).

$$S = \frac{ADC}{ADC_{\text{spe}} \cdot E} \tag{3}$$

where S is the light yield of the crystal, ADC represents the peak position of the spectrum after deducting the baseline, E is the deposited energy in the crystal, and the $ADC_{\text{spe}} =$ 8.0321 channels denote the single-photoelectron response of the Hamamatsu R6233-100 PMT at a high voltage of +1300 V. The response was calibrated using the LED-triggered charge method [36].

2.2 Measured by radioactive sources

Radioactive sources of ¹³³Ba, ¹³⁷Cs, ²⁴¹Am, ¹⁵²Eu, and ²⁰⁷Bi were employed across a range of γ-ray energies from 30.85 keV to 1063.7 keV to investigate the gamma-ray responses. The tested crystal was coupled to a Hamamatsu R6233-100 PMT via silicon oil, and the digitizer DT5751 acquired the signal waveforms in the self-triggering mode. ROOT, a data analysis framework conceived by the European Organization for Nuclear Research (CERN) [37], was used to analyze the experimental data, including baseline subtraction, fitting of the full-energy peak, and analysis of the peak position and FWHM.

2.3 Single energy X-ray measurements using the hard X-ray calibration facility

We employed two sets of hard X-ray calibration facilities (HXCF, Fig. 8) established by the National Institute of Metrology (NIM) in Beijing Changping, China [38–40] to investigate the energy responses of the three aforementioned crystals to X-rays in the 8–120 keV range. The HXCF, which plays a substantial role in the calibration of gamma-ray

Fig. 6 Resolution of Compton electrons in LaBr₃(Ce,Sr) versus the cut width in HPGe for a ¹³⁷Cs source

Fig. 7 Projected spectra of the LaBr$_3$(Ce,Sr) crystal with the HPGe ▶ energy gated at **a** 605 keV, **b** 615 keV, **c** 625 keV, and **d** 635 keV, respectively; that is, the (**a**) 56.6 keV, (**b**) 46.6 keV, (**c**) 36.6 keV, and (**d**) 26.6 keV Compton electron energy spectrum

detectors on GECAM, CubeSats, and SVOM satellites [41–43], was first built for the high-energy telescope of the HXMT as a calibration facility [44] and comprises four primary components: X-ray generator, monochromator, collimator, and standard detector. To shield stray light from the X-ray generator, the collimator features apertures of various sizes at the entrance and exit. A low-energy HPGe detector (Canberra Industries) was used as a standard. Before testing, we calibrated the HPGe detector for energy linearity, resolution, and detection efficiency using various standard radioactive sources [45].

The entire set of testing equipment, including the dataacquisition system, was placed inside an X-ray testing chamber (Fig. 9), and remotely controlled for data retrieval in a control room. The energy and flux of the X-rays were determined using an HPGe detector. The testing procedures are shown in Fig. 10. We used GENIE 2000, which is a spectroscopic data acquisition and analysis software, to record the spectral data from the HPGe detector. The crystal detector was coupled to a PMT (Hamamatsu Model CR160) using silicone oil. The signals from the crystal detector were collected using a digitizer (DT5751) and analyzed using computer software for the corresponding spectra.

The range of X-ray testing was between 8 and 120 keV in this study, with fine measurements of the absorption edge of the crystal at a step size of 0.1 keV. The performance of the crystal detector gradually changed as the X-ray energy increased, allowing for a reduced number of test energy points. Owing to testing at room temperature (22–23°C), the detector noise was slightly higher, limiting the starting test energy points to the range of 8–10 keV. For the two LaBr$_3$ crystals, the PMTs coupled to them operated at −800 V, whereas that for the NaI(Tl) crystal operated at −1000 V.

3 Results and discussion

3.1 Light yield nonlinearity to compton electrons

The light yields of the LaBr$_3$(Ce), LaBr$_3$(Ce,Sr), and NaI(Tl) crystals were normalized to "1" at an energy of 662 keV. Figure 11 demonstrates the nonlinearity of the light output of the LaBr$_3$(Ce), LaBr$_3$(Ce,Sr), and NaI(Tl) crystals to the Compton electrons within the energy range 3–400 keV. To better quantify the nonlinearity of these crystals, we introduced a metric known as the nonlinearity standard deviation (NLSD), denoted by Eq. (4), where x_i represents the relative light yield at each energy point. The NLSD values for the
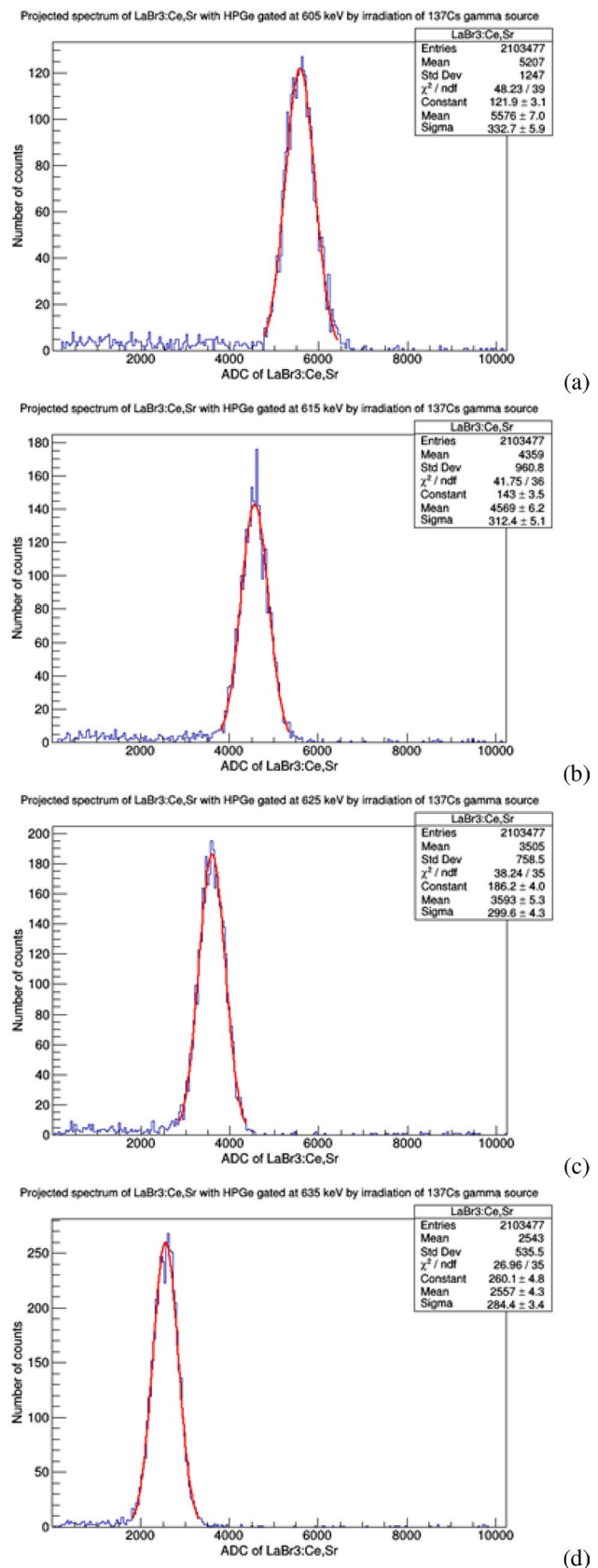

(a)

(b)

(c)

(d)

Fig. 8 (Color online) Hard X-ray Calibration Facility. Both the HPGe and crystal detectors were placed on a displacement platform and maintained on the same horizontal line
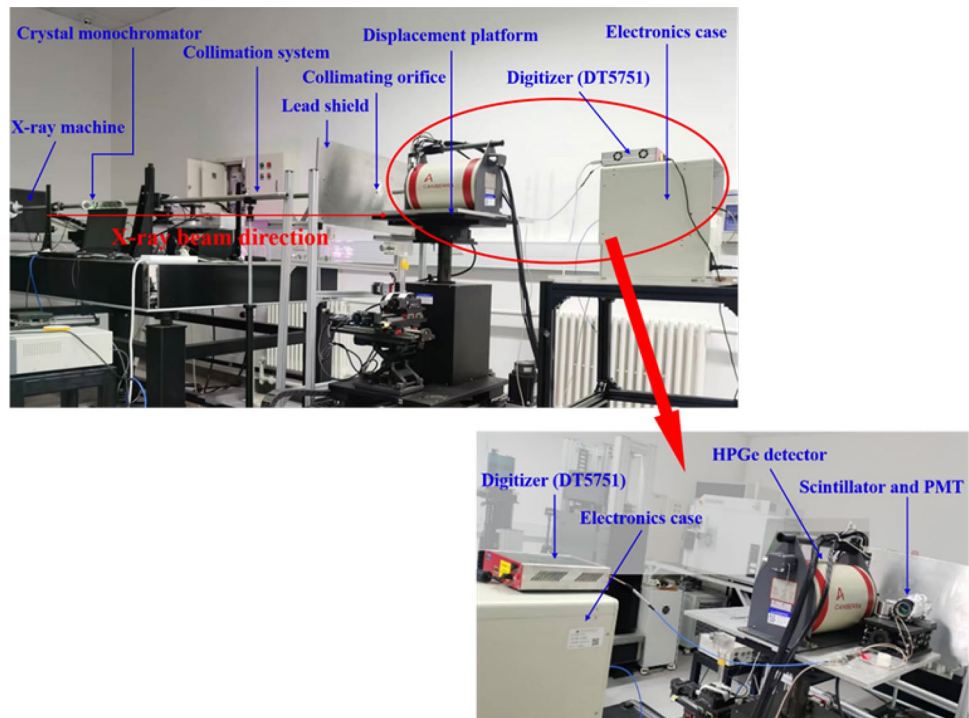

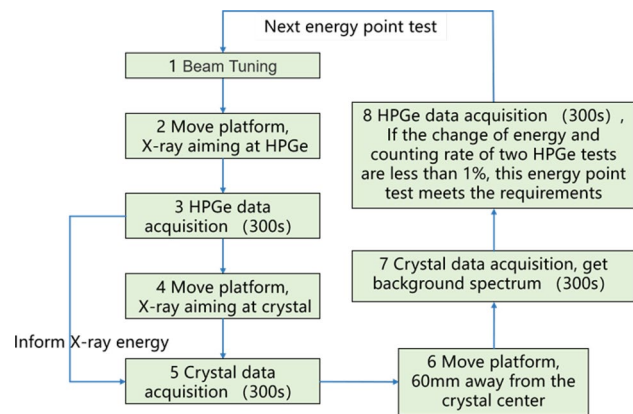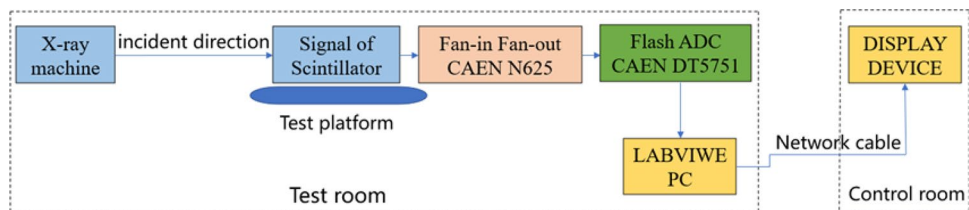**Fig. 9** Data acquisition system diagram for single-energy X-ray detection

Fig. 10 Test procedure for the nonlinear response of the crystals to X-rays

Fig. 11 Comparison of the light yield nonlinearity of LaBr$_3$(Ce), LaBr$_3$(Ce,Sr), and NaI(Tl) crystals for the 3–400 keV Compton electrons

LaBr$_3$(Ce), LaBr$_3$(Ce,Sr), and NaI(Tl) crystals were 0.11, 0.03, and 0.06, respectively. A larger NLSD value indicates a more significant nonlinearity of the crystal.

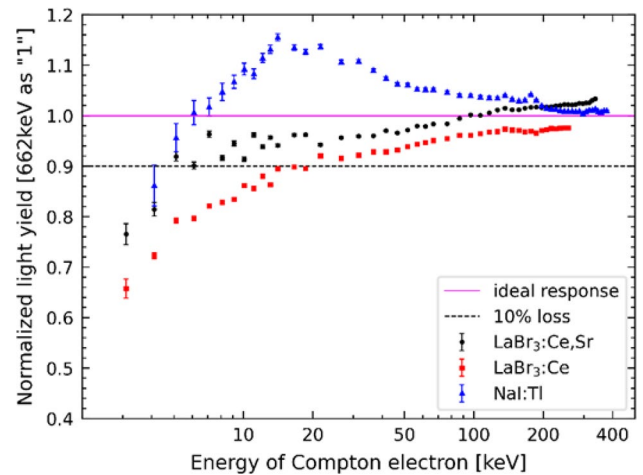$$NLSD = \sqrt{\frac{1}{n}\sum_{i=1}^{n}(x_i - 1)^2} \quad (n = 1, 2, 3...). \quad (4)$$

For both types of $LaBr_3$ crystals, as the energy of the Compton electrons decreased, the nonlinearity of the light yield gradually increased. Within the measured electron energy range, the $LaBr_3$(Ce,Sr) crystal exhibited a better linearity than that of the $LaBr_3$(Ce) crystal, particularly at energies below 20 keV. We hypothesized that the doping of Sr^{2+} may have improved the internal energy transfer mechanism within the $LaBr_3$(Ce,Sr) crystal, enhancing the energy transfer efficiency in the low-energy region, thereby ameliorating nonlinearity. Both crystals exhibited a 10% "defect" light output at approximately 5 and 20 keV, respectively. The minimum measurable energy point using WACC was 3.1 keV, at which the $LaBr_3$(Ce,Sr) crystal exhibited a "defect" of approximately 24%, whereas that of the $LaBr_3$(Ce) crystal exhibited 35%. This experiment validated the simulation results presented by Zheng et al. [17], which demonstrated the nonlinearity of the electrons, while also affirming the accuracy and rationality of both the model and experimental work conducted by the GECAM research team.

In comparison with the two $LaBr_3$ crystals, the NaI(Tl) crystal did not exhibit the monotonic "defect" of the luminescence phenomenon as the energy of the Compton electrons decreased. At approximately 14 keV, the NaI(Tl) crystal reached its maximum light yield, exhibiting an "excess" light output of approximately 15.5%. Beyond 14 keV, the light yield gradually decreased as the energy increased. Conversely, as the energy decreased to below 14 keV, the light yield decreased. The lowest test energy point was 4.1 keV, at which the NaI(Tl) crystal demonstrated a luminosity nonlinearity "defect" of approximately 14%.

3.2 The absolute light yield of crystals

The three crystals were irradiated using multiple radioactive sources to obtain the energy spectra of each crystal for different sources. The single-photoelectron responses of the Hamamatsu R6233-100 PMT used in the measurements were calibrated using the LED-triggered charge method at various voltages, enabling the calculation of the absolute

Table 2 The absolute light yield and energy resolution of crystals for the 661.6 keV gamma rays

Crystal type	Size	Light yield (ph/MeV)	Energy resolution (%)
$LaBr_3$(Ce)	1"×1"	74196	3.00±0.02
$LaBr_3$(Ce,Sr)	1"×1"	63939	3.03±0.01
NaI(Tl)	1"×1"	45445	7.18±0.07

light yields of the three crystals. The absolute light yields and energy resolutions of the samples tested at 661.6 keV are listed in Table 2.

3.3 Energy resolution

Figure 12 illustrates the energy resolution of the $LaBr_3$(Ce), $LaBr_3$(Ce,Sr), and NaI(Tl) crystals for the Compton electrons in the 3–400 keV range. The energy resolution of the NaI(Tl) crystal was comparable to that of the $LaBr_3$ crystals at 16–30 keV (Fig. 12).

The energy resolution of the crystals was expressed using the FWHM of the full-energy peak of the X-ray. Figure 13 presents the energy resolution of the $LaBr_3$(Ce,Sr), $LaBr_3$(Ce), and NaI(Tl) crystals for X-rays in the 8–100 keV range,
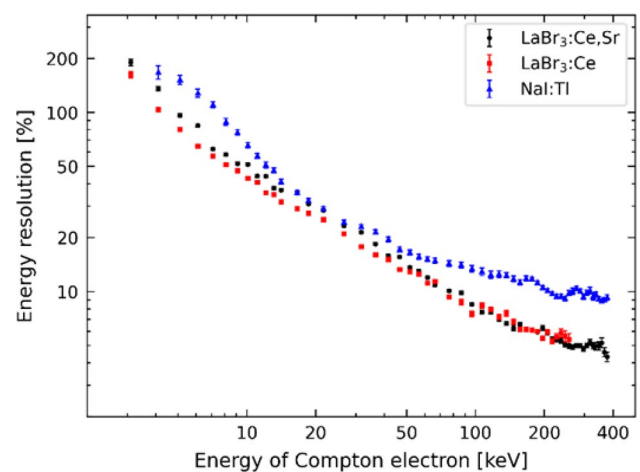
Fig. 12 Comparison of the energy resolution of the $LaBr_3$(Ce), $LaBr_3$(Ce,Sr), and NaI(Tl) crystals for the Compton electrons in the 3–400 keV range
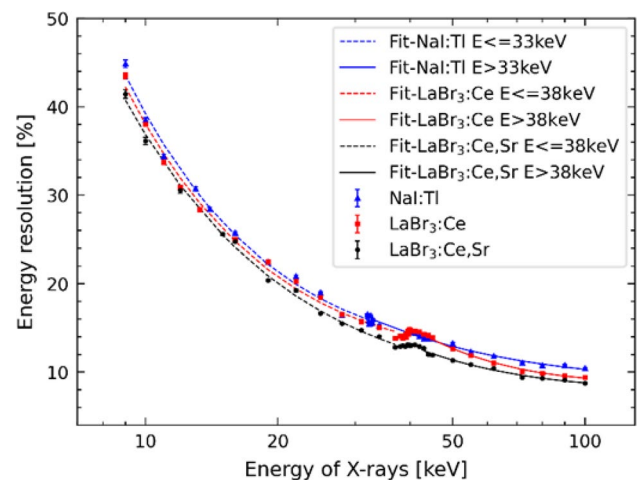
Fig. 13 Energy resolution of the $LaBr_3$(Ce,Sr), $LaBr_3$(Ce), and NaI(Tl) crystals varies with the X-ray energy

as measured by HXCF. The LaBr$_3$(Ce,Sr) crystal exhibited the best energy resolution within this energy range. At 100 keV, the resolution of the LaBr$_3$(Ce,Sr) crystal was 8.74 ± 0.0681%, whereas those of the LaBr$_3$(Ce) and NaI(Tl) crystals were 9.41±0.0976% and 10.39 ± 0.1168%, respectively. Furthermore, a slight degradation in the energy resolution, less than 1%, was observed near the binding energy of the K-shell electrons.

3.4 Comparison of the X/γ-ray and Compton electron responses

All the data in this study were standardized by setting the full-energy peak response of the 662 keV gamma rays from a ^{137}Cs source as the normalization factor. The nonlinearity of the LaBr$_3$(Ce,Sr) crystal light yield for the Compton electrons and gamma rays in the 3–1000 keV range is shown in Fig. 14. Note, the response of the Compton electrons exhibited an excellent linearity at approximately 70 keV, with a nonlinearity of less than 2%. However, a "deficiency" in the light output occurred when the energy of the Compton electrons was below 70 keV, whereas substantial nonlinearity was observed in the response to gamma rays below approximately 200 keV.

A more detailed test was conducted on the photon response below 120 keV using HXCF. Figure 14 presents the nonlinear light yield response curve of the LaBr$_3$(Ce,Sr) crystal to X-rays in the energy range of 8–120 keV. Because the error bars are similar in size to the data point symbols, they are not visible in the figure. Ideally, the relative light yield should be "1" at all energy points. However, this was not the case and varying degrees of light-yield deficiencies were observed within the tested energy range. Below 40 keV, the LaBr$_3$(Ce, Sr) crystal exhibited substantial nonlinearity

in the relative light yield response to X-rays, with the nonlinearity exceeding 10%. As the energy decreased, the slope of the curve increased, reaching a nonlinearity of 36% at 8 keV. When the X-ray energy exceeded 40 keV, the nonlinear curve approached the ideal state and the slope became milder, indicating that the fluctuation in the number of photons generated per unit energy absorbed by the LaBr$_3$(Ce, Sr) crystal was small within the energy range of 40–120 keV. The LaBr$_3$(Ce,Sr) crystal exhibited absorption edges at 13–15 keV and 38–40 keV, and a slight reduction in the relative light yield was observed within these two energy intervals.

The NLSD values for testing the LaBr$_3$(Ce,Sr) crystal with X-rays and Compton electrons were 0.17 and 0.03, respectively. The light output of the LaBr$_3$(Ce,Sr) crystal exhibited a greater nonlinearity in response to the X-rays than to the Compton electrons. This can be attributed to the different mechanisms by which these particles interact with atoms in matter. For X/γ-rays ranging from a few keV to several hundred keV, there are two possible interaction processes with the crystal: (1) a direct photoelectric cascade sequence or (2) Compton scattering followed by a photoelectric cascade sequence. These processes generate several primary electrons (e.g., Compton electrons and primary photoelectrons) and multiple secondary electrons (e.g., Auger electrons and secondary photoelectrons), with the final light emission being the sum of the contributions from secondary electrons with different energies. Notably, these electrons are the products of the interaction between the incident photons and matter, and their energies cannot exceed those of the incident particles. Therefore, the light output induced by the photons in the LaBr$_3$(Ce,Sr) crystal was always lower than that caused by the Compton electrons with equivalent energies.
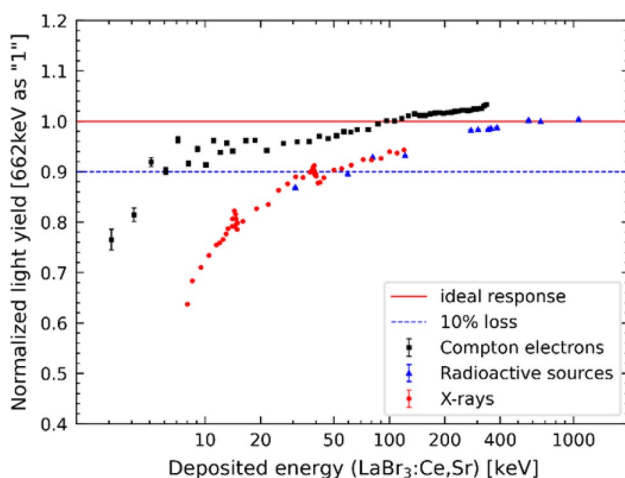

Fig. 14 Light yield nonlinearity of the LaBr$_3$(Ce,Sr) crystal for Compton electrons, gamma rays, and X-rays
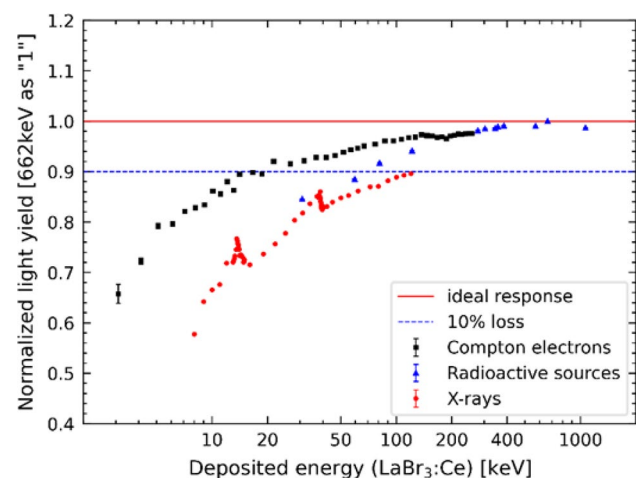

Fig. 15 Light yield nonlinearity of the LaBr$_3$(Ce) crystal for Compton electrons, gamma rays, and X-rays

We conducted detailed testing of the LaBr$_3$(Ce) crystal using the same experimental procedures and data processing methods. Figure 15 illustrates the nonlinear light-yield response of the LaBr$_3$(Ce) crystal to Compton electrons and gamma rays in the 3-1000 keV energy range. The nonlinear curves tended to be flat, and the results were similar for the Compton electrons and gamma rays when the energy was above 200 keV; however, significant differences were observed below 200 keV. As the energy decreased, the LaBr$_3$ (Ce) crystal exhibited a lower response to the full-energy peak of the gamma rays than to the Compton electrons of the same energy. This finding is consistent with the test results for the LaBr$_3$(Ce,Sr) crystal, indicating that the manner in which the particles interact with the matter directly affects the light output of the crystal. For gamma rays in the energy range of several hundred kiloelectronvolts, Compton scattering is most likely the initial interaction, and most gamma rays require multiple interactions for full absorption. The high-energy primary and secondary electrons resulting from these interactions exhibited good linear responses, reflecting the excellent linearity of the response to high-energy gamma rays.

Figure 15 demonstrates the nonlinearity curve of the LaBr$_3$(Ce) crystal to X-rays in the 8-120 keV energy range. Compared to the LaBr$_3$(Ce,Sr) crystal, this response curve deviated from the ideal state more significantly, and nearly all the measured energy points exhibited scintillation responses below 90%. The light output sharply decreased near the K-shell binding energies (13-15 keV and 38-40 keV) of Br and La, leading to a greater nonlinearity of the LaBr$_3$(Ce) crystal response curve to the X-rays. The data points below 28 keV exhibited a nonlinearity greater than 20%, and the light output at 8 keV was only 58% of the ideal state.

As the X-ray energy decreased, the induced secondary electron energies in the crystal decreased, thereby resulting in more significant light "defects". The NLSD values obtained by testing the LaBr$_3$(Ce) crystal with the X-rays and Compton electrons were 0.22 and 0.11, respectively. The LaBr$_3$(Ce) crystal exhibited a greater nonlinearity toward the X-rays and Compton electrons compared to the LaBr$_3$(Ce,Sr) crystal, particularly at energies below 100 keV. This may be attributed to the doping process, indicating that doping with Sr^{2+} ions can improve the nonlinearity of LaBr$_3$ crystals.

To better understand the differences in nonlinearity among the different types of crystals, the NaI(Tl) crystal was chosen as the third test subject (Fig. 16). Unlike the two LaBr$_3$ crystals, the NaI(Tl) crystal exhibited a pronounced "excess" response to the Compton electrons in the 8–80 keV energy range, with a nonlinearity exceeding 4%. At electron energies lower than 6 keV, the crystal displayed slight "defects" in the light output, whereas above 80 keV,
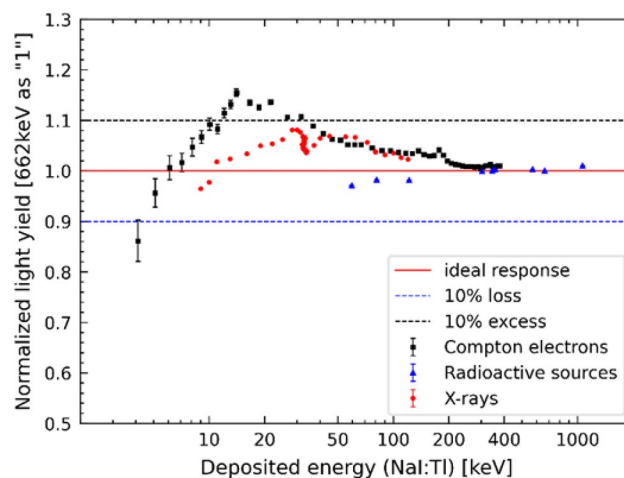

Fig. 16 Light yield nonlinearity of the NaI(Tl) crystal for Compton electrons, gamma rays, and X-rays

the curve tended to flatten, indicating a good linear response of this sodium iodide compound to high-energy electrons.

Figure 16 also demonstrates the nonlinearity of the light yield of the NaI (Tl) crystal to X-rays in the 8–120 keV energy range. Compared with the response to the Compton electrons, the X-ray test results exhibited a similar trend, with NLSD values of 0.06 for both. However, there were differences in the slopes of the curves. Direct photoelectric interactions with matter are most likely to occur for photons in the tens-of-keV range. Assuming this photoelectric absorption occurs with iodine K-shell electrons (probability of 83% when the photon energy is greater than 33.17 keV), the resulting photoelectrons have energies within the range, with a substantial "excess" light output. The total light emission induced by all secondary electrons generated from the photons exceeded that caused by Compton electrons with equivalent energies. Therefore, when the energy was within the 40–70 keV range, the NaI(Tl) crystal exhibited a higher relative light output to the X-rays, producing a greater number of photons per unit of X-ray-deposited energy compared to the case of the Compton electron incidence.

The response of the NaI (Tl) crystal to the X-rays was similar to that of the Compton electrons at approximately 33 keV, is related to the binding energy (33.17 keV) of the iodine K-shell electrons, as photons with energies lower than this cannot excite K-shell electrons from the iodine atoms. Nearly all of the photon energy was transferred to electrons, and only a small fraction of low-energy photons interacted with an iodine L-shell electron (with a binding energy of 5.19 keV) to produce lower-energy X-rays through the photoelectric effect.

Within the measured X-ray energy range, the NaI(Tl) crystal exhibited varying degrees of "excess" light output, which can also be explained by the sequence of the

photoelectric effect cascade. The low-energy electron response demonstrated an "excess" and reached its maximum value at 14 keV, as shown in Fig. 16. Therefore, when photons undergo a series of interactions to produce multiple low-energy secondary electrons, a "burst" phenomenon occurs in the light output, which also explains why the photon response reached a maximum value at approximately 30 keV instead of 14 keV. As the incident photon energy increased, the light output gradually decreased but remained above 100%, which was owing to the more complex distribution of secondary electron energies, resulting in numerous secondary electrons with energies lower than 6 keV. The electron response below 6 keV exhibited a "deficient" luminous response, which formed a so-called "compensation" effect with the "excess" phenomenon observed in the tens of keV range.

4 Conclusion

We employed the WACC technique and HXCF/radioactive sources to compare the energy responses of domestically produced LaBr$_3$(Ce), LaBr$_3$(Ce, Sr), and NaI(Tl) crystals to Compton electrons and X/γ-rays. The NLSD values obtained through the X-ray testing of the LaBr$_3$(Ce), LaBr$_3$(Ce, Sr), and NaI(Tl) crystals were 0.22, 0.17, and 0.06, respectively. In comparison, the Compton electron testing resulted in NLSD values of 0.11, 0.03, and 0.06 for the same crystals. The nonlinear curves of these domestic crystals exhibited different slopes (Figs. 14, 15 and 16), indicating varying degrees of nonlinearity at low energies. Based on the experimental results, the nonlinearity of the three crystals to the X/γ-rays exceeded that of the Compton electrons, which can be attributed to the distinct interaction mechanisms between the incident particles and material.

The NLSD values for LaBr$_3$(Ce) were 1.29 times higher for X-rays and 3.67 times higher for Compton electrons compared to LaBr$_3$(Ce, Sr), indicating that the LaBr$_3$(Ce, Sr) crystal exhibited a better linearity and that doping with Sr^{2+} ions can improve nonlinearity. However, the absolute light yield of the LaBr$_3$(Ce, Sr) crystal was slightly lower than that of LaBr$_3$(Ce) (Table 2), potentially owing to the need for further optimization of the growth process and doping ratio by domestic manufacturers. The energy resolution of our LaBr$_3$(Ce, Sr) crystal was inferior to that reported by its foreign counterparts [46]. This discrepancy may have occurred owing to the inherent performance variations among the different crystals, differences in measurement methods when coupled with PMT, or distinctions in the growth processes and raw materials between the Chinese and Saint-Gobain crystals.

The NaI(Tl) crystal exhibited an "excess" light output of up to 9.2% when tested with X-rays and 15.5% when tested with Compton electrons. This "excess" light output distinguished the NaI(Tl) crystal for having the advantage of detecting low-energy X/γ-rays. The calibration and in-orbit performance of GECAM-C validated that the NaI(Tl) crystals exceeded expectations [16, 19]. Energy resolution is not the primary concern in gamma-ray burst detection. Although NaI(Tl) crystals may not match the energy resolution and absolute light yield of LaBr$_3$ crystals, the test results demonstrated their satisfactory performance in the 10-1000 keV energy range. Furthermore, NaI(Tl) crystals can be manufactured in large sizes and are cost-effective. Consequently, GECAM-D utilizes NaI(Tl) crystals as sensitive detection materials.

We conducted a study regarding the light yield and nonlinearity of three crystals produced by the Beijing Glass Research Institute, and found that different calibration standards are required for the detection of gamma-rays and electrons. While the current GECAM satellite GRDs lack electron-gamma discrimination capabilities, the nonlinearity results of the Compton electrons may be applied to future corrections for electron detection.

Declarations

References

1. B. Abbott, R. Abbott, T. Abbott et al., Observation of gravitational waves from a binary black hole merger. Phys. Rev. Lett. **116**, 061102 (2016). https://doi.org/10.1103/PhysRevLett.116.061102

2. B. Abbott, R. Abbott, T. Abbott et al., Gravitational waves and gamma-rays from a binary neutron star merger: GW170817 and GRB170817A. Astrophys. J. Lett. **848**, L13 (2017). https://doi.org/10.3847/2041-8213/aa920c

3. B. Abbott, R. Abbott, T. Abbott et al., Gw170817: observation of gravitational waves from a binary neutron star inspiral. Phys. Rev. Lett. **119**, 161101 (2017). https://doi.org/10.1103/PhysRevLett.119.161101

4. B. Abbott, R. Abbott, T. Abbott et al., Multi-messenger observations of a binary neutron star merger. Astrophys. J. Lett **848**, L12 (2017). https://doi.org/10.3847/2041-8213/aa91c9

5. T. Li, S. Xiong, S. Zhang et al., *Insight*-HXMT observations of the first binary neutron star merger gw170817. Sci. China.-Phys. Mech. Astr. **61**, 031011 (2018). https://doi.org/10.1007/s11433-017-9107-5

6. V. Connaughton, M. Briggs, A. Goldstein et al., Localization of gamma-ray bursts using the fermi gamma-ray burst monitor. Astrophys. J. Suppl. S. **216**, 791–804 (2015). https://doi.org/10.1088/0067-0049/216/2/32

7. M. Stanbro, M. Briggs, O. Roberts et al., A fermi gamma-ray burst monitor event observed as a terrestrial gamma-ray flash and terrestrial electron beam. J. Geophys. Res.-Space. **124**, 10580–10591 (2019). https://doi.org/10.1029/2019JA026749

8. S. Xiao, S.L. Xiong, C. Cai et al., Energetic transients joint analysis system for multi-instrument (ETJASMIN) for GECAM - I. Positional, temporal, and spectral analyses. Mon. Not. R. Astron. Soc. **514**, 2397–2406 (2022). https://doi.org/10.1093/mnras/stac999

9. M. Stanbro, M. Briggs, O. Roberts et al., A study of consecutive terrestrial gamma-ray flashes using the gamma-ray burst monitor. J. Geophys. Res.-Space. **123**, 9634–9651 (2018). https://doi.org/10.1029/2018JA025710

10. S. Xiong, Special topic: Gecam gamma-ray all-sky monitor. Sci. Sin.-Phys. Mech. Astr. **50**, 129501 (2020). https://doi.org/10.1360/SSPMA-2020-0457

11. L. Lin, S. Xiao, Y. Huang et al., Observational prospects for magnetars with GECAM. Sci. Sin.-Phys. Mech. Astr. **50**, 129521 (2020). https://doi.org/10.1360/SSPMA-2019-0397

12. Y. Huang, Q. Luo, B. Zhang et al., Ultra-long gamma-ray bursts and ultra-soft gamma-ray bursts. Sci. Sin.-Phys. Mech. Astr. **50**, 129504 (2020). https://doi.org/10.1360/SSPMA-2019-0415

13. Y. Su, W. Chen, S. Xiong et al., Monitoring and research of high-energy solar flare emissions with GECAM. Sci. Sin.-Phys. Mech. Astr. **50**, 129505 (2020). https://doi.org/10.1360/SSPMA-2020-0012

14. X. Li, X. Wen, Z. An et al., The GECAM and its payload. Sci. Sin.-Phys. Mech. Astr. **50**, 129508 (2020). https://doi.org/10.1360/SSPMA-2019-0417

15. Z. An, X. Sun, D. Zhang et al., The design and performance of GRD onboard the GECAM satellite. Radiat. Detect. Technol. Methods **6**, 43–52 (2022). https://doi.org/10.1007/s41605-021-00289-y

16. D. Zhang, C. Zheng, J. Liu et al., The performance of SIPM-based gamma-ray detector (GRD) of GECAM-C. Nucl. Instrum. Methods Phys. Res. A. **1056**, 168586 (2023). https://doi.org/10.1016/j.nima.2023.168586

17. C. Zheng, W.X. Peng, X.B. Li et al., Electron non-linear light yield of LaBr$_3$ detector aboard GECAM. Nucl. Instrum. Methods Phys. Res. A **1042**, 167427 (2022). https://doi.org/10.1016/j.nima.2022.167427

18. W. Lu, L. Wang, Y. Yuan et al., Monte Carlo simulation for performance evaluation of detector model with a monolithic LaBr$_3$(Ce) crystal and SIPM array for γ radiation imaging. Nucl. Sci. Tech. **33**, 107 (2022). https://doi.org/10.1007/s41365-022-01081-3

19. C. Zheng, Z. An, W. Peng, et al., Ground calibration of gamma-ray detectors of GECAM-C. arXiv preprint arXiv:2303.00687 . https://doi.org/10.48550/arXiv.2303.00687

20. W. Wang, X. Li, J. Wu et al., Development and performance study of a dual-layer compton camera. Nucl. Tech. **46**, 030401 (2023). https://doi.org/10.11889/j.0253-3219.2023.hjs.46.030401. (**in Chinese**)

21. F. Hua, Y. Ye, X. Yang et al., Several nuclear physics experiments based on the Beijing cyclotron. Nucl. Tech. **46**, 080004 (2023). https://doi.org/10.11889/j.0253-3219.2023.hjs.46.080004. (**in Chinese**)

22. J. Zhao, S. Jiang, Y. Li et al., The contribution of 4–400 mev cosmic ray protons to the annihilation radiation in near-lunar space orbit gamma spectra. Nucl. Tech. **46**, 050201 (2023). https://doi.org/10.11889/j.0253-3219.2023.hjs.46.050201. (**in Chinese**)

23. M. Moszyski, A. Syntfeld-Kauch, L. Swiderski et al., Energy resolution of scintillation detectors. Nucl. Instrum. Methods Phys. Res. A. **805**, 25–35 (2016). https://doi.org/10.1016/j.nima.2015.07.059

24. P. Limkitjaroenporn, W. Hongtong, W. Chaiphaksa et al., The light yield non-proportionality and electron energy resolution study of CsI(tl) scintillator by Compton coincidence technique (CCT). Mat. Today-Proc. **5**, 15110–15114 (2018). https://doi.org/10.1016/j.matpr.2018.04.066

25. G. Yang, L. Hua, F. Lu et al., Response functions of a 4π summing γ detector in β-Oslo method. Nucl. Sci. Tech. **33**, 68 (2022). https://doi.org/10.1007/s41365-022-01058-2

26. V. Ranga, S. Rawat, S. Sharma et al., Intrinsic resolution of Compton electrons in CeBr$_3$ scintillator using compact CCT. IEEE T. Nucl. Sci. **65**, 616–620 (2017). https://doi.org/10.1109/TNS.2017.2779888

27. K. Roemer, G. Pausch, C. Herbach et al., A technique for measuring the energy resolution of low-z scintillators. 2009 IEEE Nuclear Science Symposium Conference Record (NSS/MIC), Orlando, FL, USA, 2009, pp. 6–11 (2009). https://doi.org/10.1109/NSSMIC.2009.5401909

28. L. Swiderski, R. Marcinkowski, M. Szawlowski et al., Non-proportionality of electron response and energy resolution of Compton electrons in scintillators. IEEE T. Nucl. Sci. **59**, 222–229 (2012). https://doi.org/10.1109/TNS.2011.2175407

29. S. Zhang, J. Xia, T. Sun et al., Transition edge sensor-based detector: from x-ray to γ-ray. Nucl. Sci. Tech. **33**, 84 (2022). https://doi.org/10.1007/s41365-022-01071-5

30. Hamamatsu (2023). https://www.hamamatsu.com.cn/cn/zh-cn/product/optical-sensors/pmt.html

31. X. Han, S. Wang, H. Wu et al., Csi-bowl: an ancillary detector for exit channel selection in γ-ray spectroscopy experiments. Nucl. Sci. Tech. **34**, 133 (2023). https://doi.org/10.1007/s41365-023-01289-x

32. Canberra (2023). https://www.mirion.com/products/technologi-es/spectroscopy-scientific-analysis

33. BEGe(2023). https://www.gammadata.se/assets/Uploads/BEGe-SS-C49318.pdf

34. X. Li, J. Ren, X. Ruan et al., Particle discrimination measurement of liquid scintillators using dt5751. Ann. Rep. Chin. Inst. Atom. En. **00**, 147 (2014) CNKI:SUN:YNXB.0.2014-00-055 (**in Chinese**)

35. X. Qian, H. Sun, C. Liu et al., Simulation study on performance optimization of a prototype scintillation detector for the grand-proto35 experiment. Nucl. Sci. Tech. **32**, 51 (2021). https://doi.org/10.1007/s41365-021-00882-2

36. Y. Wei, M. Guan, W. Xiong et al., Consistency test of PMT SPE spectrum from dark-noise pulses and led low-intensity light. Radiat. Detect. Technol. Methods **2**, 11 (2018). https://doi.org/10.1007/s41605-018-0042-6

37. H. Wu, C. Li, A root-based detector test system. Nucl. Sci. Tech. **32**, 115 (2021). https://doi.org/10.1007/s41365-021-00952-5

38. S. Guo, J. Wu, D. Hou, The development, performances and applications of the monochromatic X-rays facilities in (0.218–301) keV at NIM, China. Nucl. Sci. Tech. **32**, 14 (2021). https://doi.org/10.1007/s41365-021-00890-2

39. D. Hou, J. Wu, S. Guo et al., The realization and study of (21–301) keV monochromatic X-rays. Nucl. Instrum. Methods Phys. Res. A **927**, 382–389 (2019). https://doi.org/10.1016/j.nima.2019.02.024

40. S. Guo, Z. Jiang, J. Wu et al., Research on a tunable monochromatic x-rays source in (5~40) keV. Appl. Radiat. Isot. **181**, 110096 (2022). https://doi.org/10.1016/j.apradiso.2022.110096

41. J. He, Z. An, W. Peng et al., Ground-based calibration and characterization of LaBr$_3$-SIPM-based gamma-ray detector on GECAM satellite: 8–160 keV. Mon. Not. R. Astron. Soc. **525**, 3399–3412 (2023). https://doi.org/10.1093/mnras/stad2439

42. J. Wen, X. Zheng, J. Yu et al., Compact CubeSat gamma-ray detector for grid mission. Nucl. Sci. Tech. **32**, 99 (2021). https://doi.org/10.1007/s41365-021-00937-4

43. X. Wen, J. Sun, J. He et al., Calibration study of the gamma-ray monitor onboard the SVOM satellite. Nucl. Instrum. Methods Phys. Res. A. **1003**, 165301 (2021). https://doi.org/10.1016/j.nima.2021.165301

44. X. Li, C. Liu, Z. Chang et al., Ground-based calibration and characterization of the He detectors for *Insight*-HXMT. J. High. Energy Astrophys. **24**, 6–14 (2019). https://doi.org/10.1016/j.jheap.2019.09.003

45. L. Haoran, W. Jinjie, L. Juncheng et al., Lege detector intrinsic efficiency calibration for parallel incident photons. Appl. Radiat. Isot. **109**, 551–554 (2016). https://doi.org/10.1016/j.apradiso.2015.11.1023

46. M. Alekhin, J. Haas, I. Khodyuk et al., Improvement of γ-ray energy resolution of Labr$_3$:Ce^{3+} scintillation detectors by Sr^{2+} and Ca^{2+} co-doping. Appl. Phys. Lett. **102**, 161915 (2013). https://doi.org/10.1063/1.4803440